Understanding patterns of haemorrhage in the eye

Richard Bonshek, Stephen Cowley, Oliver Jensen,
Philip Pearce, Anusha Ravi, Peter Stewart,
Robert Whittaker, Moussa Zouache

January 11, 2016

Abstract

We examine a potential mechanism of localised bleeding in the optic nerve sheath arising from head injury in infants. We consider how a rapid deformation of the skull leads to a rapid rise in intracranial pressure, which in turn creates a disturbance that propagates along the cerebrospinal fluid (CSF) in the optic nerve sheath subarachnoid space (ONSAS). The skull is modelled mathematically as a set of hinged plates and the ONSAS as a collapsible fluid-filled channel. Our model predicts that the propagating disturbance steepens into a shock at its leading edge, and that reflection of the disturbance at the closed end of the ONSAS leads to locally elevated CSF pressure. This may provide a mechanistic explanation for bleeding in the ONSAS close to the back of the eye. Our study demonstrates how mathematical modelling can provide insights into mechanisms of trauma in situations where human or animal experiments are inappropriate.

1 Introduction

Patterns of retinal bleeding are important signatures of injury or disease, and retinal haemorrhage (RH) is a prominent feature in cases of non-accidental head injury (NAHI) in children. However, there is disparity between clinical observations of RH and most biomechanical approaches to thresholds of retinal vascular damage [4]. In addition, RH can occur due to elevated intracranial pressure and elevated vascular pressure, with retinal pathology in Terson's syndrome, seen in situations of precipitate rise in intracranial pressure (ICP) (such as due to rupture of an intracranial arteriovascular malformation or arterial aneurysm), having the greatest similarity to the RH and retinal perimacular folds of NAHI and severe accidental head injury [13, 20].

Retinal pathology in Terson's syndrome is frequently accompanied by optic nerve sheath (ONS) bleeding [14] as in many cases of NAHI [8]. However blood does not enter the ONS directly from the cranial compartment, despite a direct connection between the intracranial cerebrospinal fluid (CSF) space surrounding the brain and the optic nerve subarachnoid space (ONSAS) in the meningeal layer of the ONS [19]. Instead, the severe elevation in ICP is communicated to the CSF in the ONSAS, where the blood vessels bridging this space are exposed to the increase in pressure and are hence vulnerable to rupture. The central retinal vein (CRV) may be particularly vulnerable to compression as it traverses the ONSAS space as it exits the optic nerve. Central retinal vein occlusion (CRVO), accompanied by the reflex arterial pressure elevation due to raised intracranial pressure, may then lead to the retinal pathology [14].

In order to gain insight into a possible mechanism for localized ONS bleeding, we consider here a scenario in which a sudden rise in intracranial pressure (ICP), associated with traumatic head injury in an infant, generates a disturbance in the CSF in the ONSAS, leading to locally elevated pressures at its distal end. We use an idealised mathematical model of the infant skull to estimate the rise in ICP, and model the ONSAS as a collapsible fluid-filled channel to consider how the pressure disturbance propagates towards the back of the eye. We consider infants at an age when the skull plates have yet to fuse. We assume the overall deformation of the skull is determined by the bending resistance between the skull plates. For such infants we focus on a sudden impact to the head, as might be the case in a head-on car crash with the infant in a rear-facing child seat. In a severe crash RH has been observed. In cases of repeated oscillation of the infant's head, we consider the effect of abrupt deceleration of the head during one oscillation.

In detail, the sequence of events that we envisage is as follows:

- the impact to head causes a sudden rise in intracranial pressure (ICP), associated with deformation of the soft infant skull;
- the rise in CSF pressure is transmitted to the CSF occupying the optic nerve sheath (within the ONSAS) outside the skull;
- the pressure rise generates a wave of CSF that propagates along the ONSAS, steeping at its front into an elastic jump;
- the wave accumulates fluid behind its leading edge and then reflects from the closed end of the ONS near the back of the eye;
- the pressure is elevated at the reflection site, so expanding/stretching the dura and causing damage to blood vessels that span the ONSAS (alternatively damage to the blood vessels might be ascribed either to the relatively rapid flow of CSF past them, or to viscoseleastic effects because of the rapid expansion).

This concept relates to studies by [2] on syringomyelia which also ascribe damage to reflection of an elastic jump at a blockage in the spinal column.

2 Background

2.1 Anatomy

The eye and the brain are directly connected by the optic nerve, where long bundles of axonal fibres transmit signals from the retina to the thalmus. The optic nerve measures approximately 3mm in diameter and approximately 40mm in length, exceeding the total length of the orbit by about a factor of one third; the slackness allows for free rotation of the eyeball.

The meningeal tissue surrounding the brain is deflected around the optic nerve providing direct communication with the CSF spaces in the brain. This meningeal tissue forms the ONS and comprises four concentric layers: the pia, the ONSAS, the dura and a layer of fat (see figure 1). The pia mater is adhered to the outside of the optic nerve while the dura mater is externally surrounded by fatty tissue forming a cushion for the eye inside the orbit. The arachnoid membrane is attached to the interior surface of the the dura, and confined between this and the pia is the ONSAS, which is filled with CSF. However, this CSF space terminates at the level of the lamina cribrosa/sclera, and so any flow along the CSF space toward the eye must be reflected back toward the brain. The ONSAS has a width of approximately H=0.5–1.2mm [21], however it widens anteriorly before terminating.

2.2 Stiffnesses and elasticities

The Young's modulus of bone in the skull rises from around 2GPa at birth to 6GPa at age 6 [17]. The Young's modulus E for a suture under stretch has been estimated to be 1/35 of the bone modulus [5], giving $E_{suture} \approx 5 - 15MPa$. The brain is substantially softer: we assume here that $E_{brain} \approx 350$Pa. To estimate the bending stiffness of a suture, use the three-point bending test result

$$E = \frac{F}{d}\frac{L^3}{4wh^3} \tag{1}$$

where F is the applied force, d the deflection, L the distance between supports, w the sample width and h the sample thickness. The work done is then

$$Fd = E_{suture} 4wh^3 \frac{\theta^2}{L} = \tfrac{1}{2} K w \theta^2 \tag{2}$$

where $\theta \sim d/L$ is the deflection angle and $K = 8E_{suture}h^3/L$ a constant representing the stiffness of the suture per unit length. With $E_{suture} = 10$MPa, $h = 2$mm and $L = 2$mm, we estimate the stiffness per unit length of the suture to be $K \approx 80$ Pa m^2. Additional parameters are listed in Table 1.

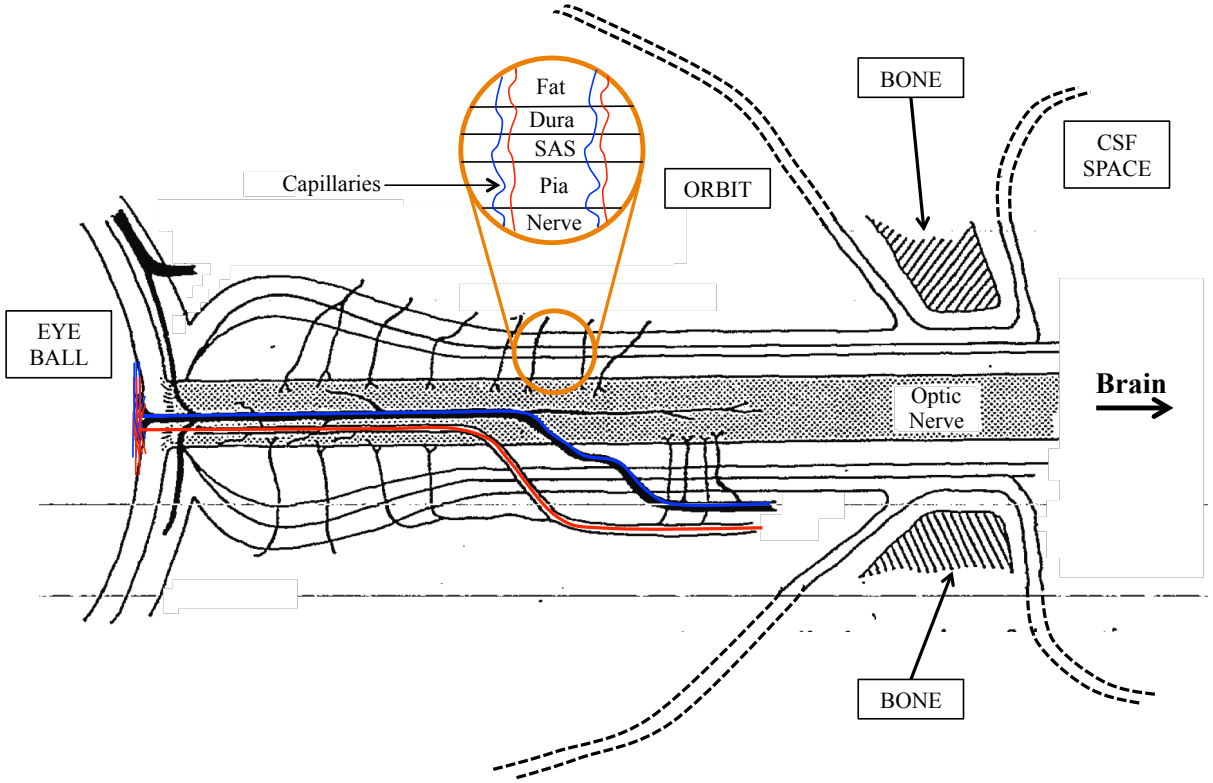

Figure 1: Schematic of the optic nerve and the surrounding sheath. *SAS: subarachnoid space.*

Parameter	**Symbol**	**Typical Value**
Skull radius	a	0.1 m
Skull Youngs modulus	E_{bone}	10 MPa
Brain Young's modulus	E_{brain}	350 Pa
Brain density	ρ	10^3 kg m^{-3}
Skull Suture bending stiffness (per unit length)	K	80 Pa m^2
ONSAS thickness	h_0	0.7mm
baseline CSF pressure	p_0	12mmHg
ONSAS length	L	27mm
density of CSF	ρ_c	1000 kg m^{-3}
viscosity of CSF	μ	0.001 Pa s
stiffness parameter of dura	K_d	fitted
elastic tension in dura	T_d	unknown
baseline diameter of the optic nerve	D_{on}	3mm
baseline diameter of the optic nerve sheath	D_{ons}	4.4mm

Table 1: Table of key parameters.

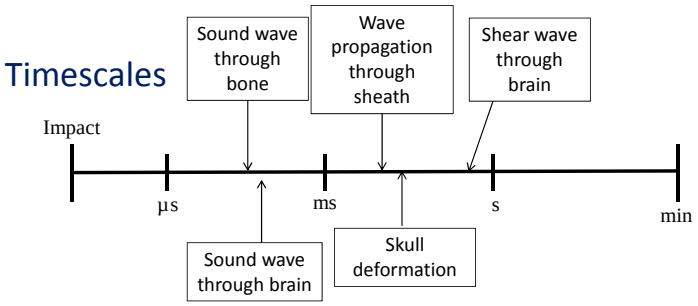

Figure 2: A schematic diagram illustrating relevant timescales.

2.3 Timescales

We identify the following timescales in the problem (see figure 2).

- The time for a sound wave to propagate 10cm through bone, based on a sound speed 4000m/s, is 0.25×10^{-4} s.
- The time for a sound wave to propagate 10cm through water (brain), based on a sound speed 1500m/s, is approx 10^{-4} s.
- The timescale for a wave to propagate 25mm along the ONS is 0.01s: we estimate this by assuming the wavespeed to be similar to an artery at 2.5m/s (from compliance data; see below).
- The timescale of skull deformation when oscillating at its fundamental frequency is estimated below to be around 10^{-2} s.
- The wavespeed in brain tissue (elastic shear wave) is $(E_{brain}/\rho)^{1/2} \approx 0.5\,\mathrm{m/s}$ for $E_{brain} = 350\,\mathrm{Pa}$, $\rho = 10^3\,\mathrm{kgm}^{-3}$. The time for a wave to propagate 10cm through brain tissue is approx 0.2s.
- For flow through the short gap between the optic nerve and bone, the time for viscous effects to be significant when pressure is ramped suddenly is $\rho_c h^2/\mu$; for CSF (water) in a gap of 0.2 mm, the viscous penetration time is 4 s. So the flow in this gap can be treated as inviscid.

We therefore focus on events taking place on timescales of order 0.01s, over which pressure is expected to rise in the skull after an impact and waves to propagate along the ONS.

The upstream boundary condition for the collapsible sheath is $p_1 = p_{brain} - L\rho u_{1t}$, if one accounts for unsteady inertia in the segment of length L adjacent to bone. The pressures arising over a time of 0.01s are order 100Pa for speeds of 1m/s over a distance 1mm, which is substantially smaller than the rise in CSF. Therefore we ignore the unsteady inertia of the fluid in this gap. (It may however be necessary to account for viscous losses where the optic nerve passes through the skull.)

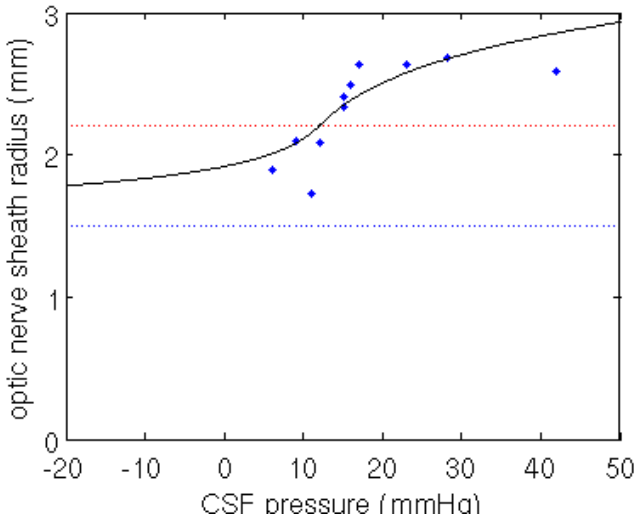

Figure 3: Measurements of the radius of the dural sheath as a function of CSF pressure (blue filled circles) along with fitted constitutive model for the dura tissue with $H = 0.7$mm at $p_0 = 12$mmHg (black line). The blue dotted line represents the optic nerve and the red dotted line represents the baseline position of the dural sheath.

2.4 Constitutive model for the dura mater

To fit a constitutive law for the dura using the data obtained by [1] and plotted as filled blue circles in Fig. 3, we assume an exponential relationship between CSF pressure and ONS diameter D_{ons}.

We relate this to the thickness of the ONSAS by writing $D_{ons} = 2h + D_{on}$, where D_{on} is the diameter of the optic nerve. We then define the displacement of the the dura from its baseline as $d = h - H$, where H is the baseline width of the ONSAS. In general H is a function of the position along the ONSAS, but in this section we assume $H = h_0$, a constant.

We assume that the constitutive law for the width of the ONSAS takes the form

$$\mathcal{P} = \begin{cases} p_0 + K_d(\exp(\alpha d) - 1), & d > 0, \\ p_0 + (K_d H/h)\exp(-\alpha d), & d < 0. \end{cases} \tag{3a}$$

We perform least squares fitting for the two unknowns α and K based on the data of [1]. For $h_0 = 0.7$mm at a CSF pressure of $p_0 = 12$ mmHg [21] we estimate

$$K_d = 6.510\text{mmHg}, \qquad \alpha = 1.314\text{mm}^{-1}, \tag{4}$$

shown as the black line on Fig. 3.

3 CSF pressure perturbation from a traumatic event

The skull comprises a number of relatively rigid plates which fuse together as the child grows. The brain and other material in the skull cavity is almost incompressible but relatively easy to deform in a volume-conserving manner. It is clear that a sudden acceleration or deceleration of the skull (or some part of it) will result in pressure changes within the brain. Physically, there are a number of mechanisms which can cause these changes:

1. a uniform pressure change δp_g in response to a global compression, or to satisfy global incompressibility;

2. a pressure change δp_a that is varies linearly in space (i.e. has a uniform gradient) in order to provide a uniform acceleration or deceleration of the skull and brain;

3. a spatially varying pressure change δp_i to satisfy local compression / incompressibility in response to local inertial forces in the brain;

4. a spatially varying pressure change δp_e to satisfy local compression / incompressibility in response to elastic shear forces.

We estimate the size of the last three pressures below.

3.1 Order-of-magnitude estimates

We model the skull as a relatively hard but hinged spherical shell of radius a, containing an incompressible elastic material of density ρ and Young's modulus E. The skull plates are considered rigid, with the sutures between them having a bending stiffness K per unit length, and the total length of suture is $O(a)$. The skull is assumed to be moving at velocity V before being brought to an abrupt halt by a collision with a stationary rigid blunt object.

During the impact, the skull and brain will deform. We use energy arguments to estimate the maximum possible deformation, and the natural frequency of the resulting oscillations, before using these to obtain estimates of the sizes of the various forces and pressures produced.

The initial kinetic energy T of the skull and brain is estimated by

$$T \sim \rho a^3 V^2 \,. \tag{5}$$

Suppose that the maximum deformation of the sphere is ϵa, and thus the plate sutures bend by an angle $\theta = O(\epsilon)$, and the brain undergones a strain of $O(\epsilon)$. For the worst-case scenario, we assume that at the maximum deformation, all the initial kinetic energy has been converted into elastic energy U_s in the skull sutures and U_b in the brain. Since there is a length of $O(a)$ of sutures, and a volume of $O(a^3)$ of brain, the energies are estimated as follows:

$$U_s \sim a \cdot K \cdot \theta^2 \sim \epsilon^2 a K \,, \qquad U_b \sim a^3 \cdot E \cdot \epsilon^2 \sim \epsilon^2 a^3 E \,. \tag{6}$$

Provided $K \gg a^2 E$ (which is verified below) the skull energy will dominate, and hence $T \sim U_s$, which gives

$$\epsilon^2 \sim \frac{\rho a^2 V^2}{K} \,. \tag{7}$$

The natural oscillations of the skull in this deformation mode will then be due to a balance of the forces from the skull-plate sutures and inertia within the brain. The torque from the sutures will be $K\theta$ per unit length. The mass to be moved is ρa^3. If the oscillations have frequency ω, then the acceleration scales like $\epsilon a \omega^2$. Newton's second law then gives

$$a \cdot \frac{1}{a} \cdot K\epsilon \sim \rho a^3 \cdot \epsilon a \omega^2 \qquad \Rightarrow \qquad \omega^2 \sim \frac{K}{\rho a^4} \,. \tag{8}$$

In (41) below we provide a more precise estimate of this frequency.

The deceleration at the impact will occur on the same timescale as the natural oscillations. The pressure difference δp_a associated with this will therefore be

$$\frac{\delta p_a}{a} \sim \rho \omega V \qquad \Rightarrow \qquad \delta p_a \sim \frac{\sqrt{\rho K} V}{a} \,. \tag{9}$$

The pressure differences δp_i associated with the inertia of the brain is estimated as

$$\frac{\delta p_i}{a} \sim \rho \epsilon a \omega^2 \qquad \Rightarrow \qquad \delta p_i \sim \frac{\sqrt{\rho K} V}{a} \,, \tag{10}$$

which is the same scale as δp_a. The pressure difference δp_e associated with elastic shear forces in the brain is estimated as

$$\frac{\delta p_e}{a} \sim \frac{\epsilon E}{a} \qquad \Rightarrow \qquad \delta p_e \sim \frac{\sqrt{\rho K} V}{a} \cdot \frac{a^2 E}{K} \,, \tag{11}$$

which will be small compared with the other two pressures provided $a^2 E \ll K$.

From the values in table 1, we obtain $a^2 E / K \sim 0.04$ (taking $E = E_{brain}$), so we do indeed have $a^2 E \ll K$.

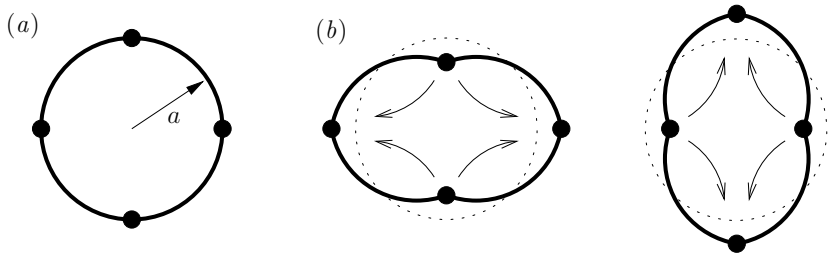

Figure 4: A depiction of the simple hinged skull model considered in §3.2. (a) The skull in its natural circular configuration. (b) The single mode of oscillation, with its two extreme configurations.

From (7) and the values in table 1, we have $\epsilon \sim 0.35(V\,/\,\mathrm{ms}^{-1})$. This is too large for physically reasonable speeds and deformations. So either the sutures must be stronger than expected, geometric constraints in the 3D deformations lead to some additional resistance, or the resistance of the brain to deformations must be larger than expected at larger deformations.

From (8) and the values in table 1, we have $\omega \approx 30\,\mathrm{s}^{-1}$ to be the resonant frequency of the skull oscillation. This frequency is significantly higher than that expected in shaking-induced injury, suggesting there is unlikely to be a resonant interaction. However shaking may lead to rapid decelerations of the head at the end of each cycle, which can be expected to induce rapid pressure changes over a timescale $1/\omega$.

3.2 Simple model for oscillations of a 2D hinged skull

In this section, we make these estimates more precise by determining the frequency of the normal mode of oscillation for a simple model of a hinged skull surrounding an elastic brain.

We assume that the skull is initially a thin circular shell of interior radius a and is made of four rigid hinged plates, each occupying $\frac{1}{4}$ of the circumference, as shown in figure 4. The hinges are sprung, and exert a torque equal to K times the angular deflection from their natural configuration. The inside of the skull is filled with a uniform incompressible linearly elastic material, with density ρ and Young's modulus E.

We use both cartesian coordinates (x, y) and polar coordinates (r, θ), and assume that the deformations are small. The vector displacement of the material point initially at (a, θ) on the skull is described by $\boldsymbol{\delta}(\theta, t)$. The interface conditions between the skull and the interior are linearised back to $r = a$.

3.2.1 Interior equations and boundary conditions

As discussed above, we assume that the normal mode oscillations will be on a timescale T such that

$$\frac{T^2 E}{\rho a^2} \ll 1 \tag{12}$$

This ensures that the motion will be inertia-dominated, and elastic shear forces can be neglected. The governing equations for the displacement $\boldsymbol{u}$ and pressure p in the interior are then

$$\rho \frac{\partial^2 \boldsymbol{u}}{\partial t^2} = -\boldsymbol{\nabla} p\,, \tag{13}$$

$$\boldsymbol{\nabla} \cdot \boldsymbol{u} = 0\,. \tag{14}$$

subject to

$$\boldsymbol{u} \cdot \hat{\boldsymbol{r}} = \boldsymbol{\delta} \cdot \hat{\boldsymbol{r}} \quad \text{on} \quad r = a\,. \tag{15}$$

Thus the interior behaves like an inviscid fluid. We would expect some elastic shear layers adjacent to the boundary, in order to allow the imposition of a tangential displacement boundary condition. In practice, since the brain is surrounded by a layer of CSF, it would be more appropriate to apply stress-free conditions there. Thus the shear layers will be weak, and we shall neglect them in the calculations that follow.

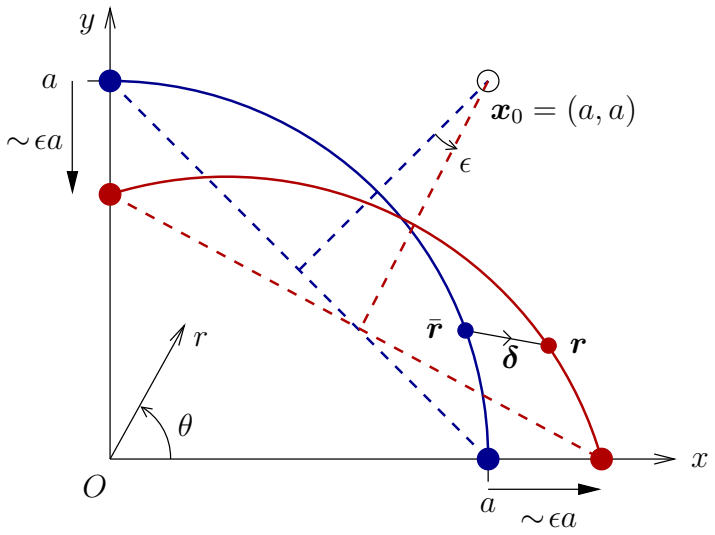

Figure 5: The motion of a single plate undergoing a rotation of angle ϵ about the point $\boldsymbol{x}_0$, within the linearised approximation for $\epsilon \ll 1$. A general initial point $\bar{\boldsymbol{r}}(\theta)$ on the skull is displaced by $\boldsymbol{\delta}(\theta)$ to lie at new position $\boldsymbol{r}(\theta)$.

In the usual way, we take the divergence of (13) and apply (14), so obtain a field equation for the pressure:

$$\nabla^2 p = 0 \tag{16}$$

Using (13), the kinematic boundary condition (15) becomes:

$$\frac{\partial p}{\partial r} = \frac{\partial^2 \boldsymbol{\delta}}{\partial t^2} \cdot \hat{\boldsymbol{r}} \tag{17}$$

We also need a dynamic boundary condition, which says that the traction $\boldsymbol{\tau}$ on the skull is given by pressure

$$\boldsymbol{\tau} = p\hat{\boldsymbol{r}}\,. \tag{18}$$

(There is no tangential traction because of the assumption of a thin CSF layer surrounding the brain.)

3.2.2 Plate Motion

The four skull plates can oscillate only in a single mode. The deformation has one degree of freedom only, which we describe by $\epsilon(t)$, the angle through which each of the plates rotates.

We consider just the plate in the first quadrant as shown in figure 5; the others will follow by symmetry. For small amplitude deformations, the plate effectively rotates about the point $\boldsymbol{x}_0 = (a, a)$, with infinitesimal rotation matrix

$$\mathcal{R}_\epsilon = \begin{pmatrix} 1 & -\epsilon \\ \epsilon & 1 \end{pmatrix} \tag{19}$$

The initial and deformed positions of a material point initially at angle θ are given by

$$\bar{\boldsymbol{r}} = a \begin{pmatrix} \cos\theta \\ \sin\theta \end{pmatrix}, \qquad \boldsymbol{r} = \mathcal{R}_\epsilon(\bar{\boldsymbol{r}} - \boldsymbol{x}_0) + \boldsymbol{x}_0. \tag{20}$$

Then the deformation is given by

$$\boldsymbol{\delta} = \boldsymbol{r} - \bar{\boldsymbol{r}} = \mathcal{R}_\epsilon(\bar{\boldsymbol{r}} - \boldsymbol{x}_0) - (\bar{\boldsymbol{r}} - \boldsymbol{x}_0) = (\mathcal{R}_\epsilon - \mathcal{I})(\bar{\boldsymbol{r}} - \boldsymbol{x}_0). \tag{21}$$

Putting in the values we get

$$\boldsymbol{\delta} = a \begin{pmatrix} 0 & -\epsilon \\ \epsilon & 0 \end{pmatrix} \begin{pmatrix} \cos\theta - 1 \\ \sin\theta - 1 \end{pmatrix} = \epsilon a \begin{pmatrix} -\sin\theta + 1 \\ \cos\theta - 1 \end{pmatrix}. \tag{22}$$

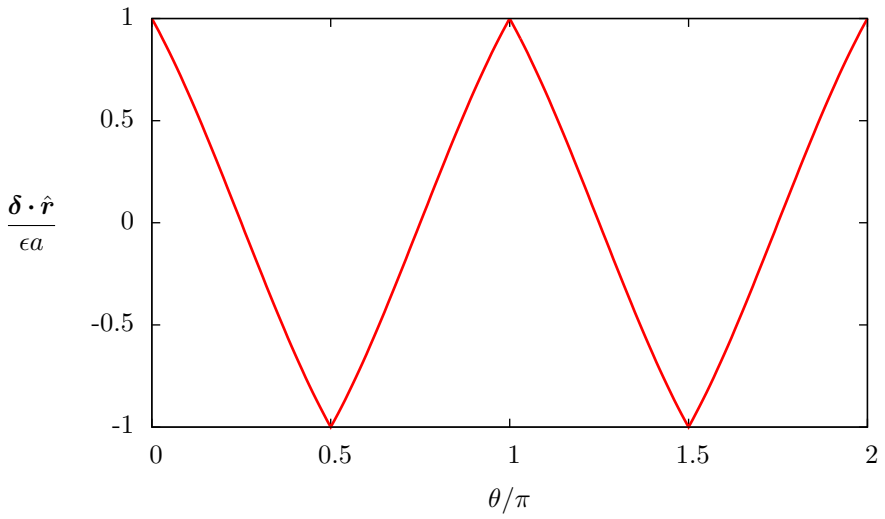

Figure 6: The linearised normal displacements of the skull under the simple hinged model, when each plate rotates by a small angle ϵ. The curve is plotted by extending (23) to the full range of θ using symmetry.

The normal component of the displacement is then

$$\begin{aligned}\boldsymbol{\delta}\cdot\hat{\boldsymbol{r}} &= \epsilon a \begin{pmatrix} -\sin\theta + 1 \\ \cos\theta - 1 \end{pmatrix} \cdot \begin{pmatrix} \cos\theta \\ \sin\theta \end{pmatrix} \\ &= \epsilon a(\cos\theta - \sin\theta) \\ &= -\epsilon a\sqrt{2}\sin(\theta - \pi/4)\,. \end{aligned} \tag{23}$$

This is extended by symmetry to the full range $0 \le \theta < 2\pi$. The resulting function is shown in figure 6.

3.3 Interior solution

The general solution to Laplace's equation in 2D polar coordinates can be written as

$$p = \sum_{n=0}^{\infty} r^n \left[a_n \cos\Big(n(\theta - \pi/4)\Big) + b_n \cos\Big(n(\theta - \pi/4)\Big)\right]\,. \tag{24}$$

Because of the symmetry of the boundary forcing, we can drop some of the terms from the sum. It is also convenient to introduce a number of pre-factors. We therefore write our ansatz as

$$p = \ddot{\epsilon}\rho a^2 \sum_{n=0}^{\infty} b_n \left(\frac{r}{a}\right)^{4n+2} \sin\Big((4n+2)(\theta - \pi/4)\Big)\,. \tag{25}$$

From this and (23), the boundary condition (17) then becomes

$$\sum_{n=0}^{\infty} b_n(4n+2)\left(\frac{r}{a}\right)^{4n+1} \sin\Big((4n+2)(\theta - \pi/4)\Big) = \sqrt{2}\sin(\theta - \pi/4) \tag{26}$$

for $0 < \theta < \pi/2$. Treating this as a half-wave Fourier series, and writing $\phi = \theta - \pi/4$, the coefficients can be written as

$$b_n = \frac{4\sqrt{2}}{\pi(4n+2)} \int_{-\pi/4}^{\pi/4} \sin(\phi)\,\sin\Big((4n+2)\phi\Big)\,\mathrm{d}\phi\,, \tag{27}$$

$$= \frac{4\sqrt{2}}{\pi(4n+2)} \int_{0}^{\pi/4} \cos\Big((4n+1)\phi\Big) - \cos\Big((4n+3)\phi\Big)\,\mathrm{d}\phi \tag{28}$$

$$= \frac{8(-1)^n}{\pi(4n+1)(4n+2)(4n+3)}. \tag{29}$$

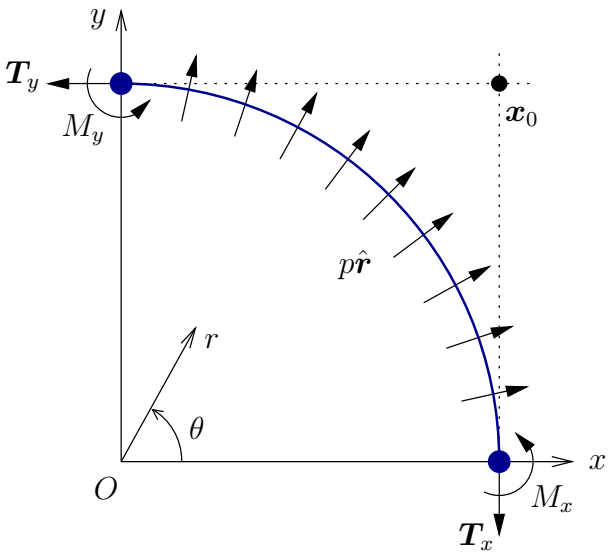

Figure 7: The various forces and moments acting on a skull plate from the hinges and the interior.

Thus, in the interior,

$$p = \ddot{\epsilon}\rho a^2 \sum_{n=0}^{\infty} \frac{8(-1)^n}{\pi(4n+1)(4n+2)(4n+3)} \left(\frac{r}{a}\right)^{4n+2} \sin\Big((4n+2)(\theta-\pi/4)\Big)\,. \tag{30}$$

From (18), the traction exerted on the skull plates at $r = a$ is

$$\boldsymbol{\tau} = \ddot{\epsilon}\rho a^2 \sum_{n=0}^{\infty} \frac{8(-1)^n}{\pi(4n+1)(4n+2)(4n+3)} \sin\Big((4n+2)(\theta-\pi/4)\Big)\,\hat{\boldsymbol{r}}\,. \tag{31}$$

3.4 Moment balance on a skull plate

In order to close the problem, we must apply Newton's second law to each of the skull plates. We assume that the inertia of the pates is negligible (compared to that in the interior), so that the forces and moments on each plate are always in equilibrium.

The various forces and moments acting on the plate are shown in figure 7. These are, the traction $\boldsymbol{\tau}(\theta)$ from the fluid, contact forces T_x and T_y at the joints, and moments M_x and M_y at the joints. The forces must be in the directions shown by symmetry. Their values are set by appropriate integrals of the traction over the plate. It is thus convenient to take moments about the point $\boldsymbol{x}_0$ to avoid contributions from these forces.

The equilibrium equation is then

$$G + M_x + M_y = 0 \tag{32}$$

where $M_x = M_y = -2K\epsilon$ are the moments from the hinges, and G is the total moment about $\boldsymbol{x}_0$ from the traction τ. Geometrically, we see that G is given by

$$G = -\sqrt{2}a \int_0^{\pi/2} (\boldsymbol{\tau}\cdot\hat{\boldsymbol{r}})\,\sin(\theta-\pi/4)\,a\mathrm{d}\theta\,. \tag{33}$$

Substituting for $\boldsymbol{\tau}$ from (31), and again writing $\phi = \theta - \pi/4$, we have

$$\begin{aligned} G &= -\frac{8\sqrt{2}\ddot{\epsilon}\rho a^4}{\pi} \sum_{n=0}^{\infty} \int_{-\pi/4}^{\pi/4} \frac{(-1)^n \sin\bigl((4n+2)\phi\bigr) \sin(\phi)}{(4n+1)(4n+2)(4n+3)} \,\mathrm{d}\phi\,, && (34)\\ &= -\frac{8\sqrt{2}\ddot{\epsilon}\rho a^4}{\pi} \sum_{n=0}^{\infty} \int_{0}^{\pi/4} (-1)^n \frac{\cos\bigl((4n+1)\phi\bigr) - \cos\bigl((4n+3)\phi\bigr)}{(4n+1)(4n+2)(4n+3)} \,\mathrm{d}\phi\,, && (35)\\ &= -\frac{16\ddot{\epsilon}\rho a^4}{\pi} \sum_{n=0}^{\infty} \frac{1}{(4n+1)^2(4n+2)(4n+3)^2}\,, && (36)\\ &= -\frac{4(\mathcal{C} - \log 2)\ddot{\epsilon}\rho a^4}{\pi} && (37) \end{aligned}$$

where $\mathcal{C} = 0.915\ldots$ is Catalan's constant.

The equilibrium equation (32) then becomes

$$\frac{4(\mathcal{C} - \log 2)\ddot{\epsilon}\rho a^4}{\pi} + 4K\epsilon = 0 \tag{38}$$

or

$$\ddot{\epsilon} + \left(\frac{\pi K}{(\mathcal{C} - \log 2)\rho a^4}\right)\epsilon = 0\,. \tag{39}$$

This represents simple harmonic motion, with general solution

$$\epsilon(t) = \epsilon_0 \cos(\omega(t - t_0))\,, \tag{40}$$

where ϵ_0 is the amplitude and t_0 a phase factor, and the frequency ω is given by

$$\omega = \sqrt{\frac{\pi K}{(\mathcal{C} - \log 2)\rho a^4}}\,. \tag{41}$$

As anticipated in the scaling argument above, in order for the assumption (12) to hold with $T \sim \omega^{-1}$, we find we need

$$\frac{a^2 E}{K} \ll 1\,. \tag{42}$$

This can be interpreted physically as the elastic interior being much softer than the hinges between the skull plates.

3.4.1 Pressure and motion inside the skull

Using (25) and the solution (40) for $\epsilon(t)$, the pressure inside the skull is given by

$$\begin{aligned} p \;=\; & -\epsilon_0 \rho a^2 \omega^2 \frac{8}{\pi} \cos\Bigl(\omega(t - t_0)\Bigr) \\ & \times \sum_{n=0}^{\infty} \frac{(-1)^n}{(4n+1)(4n+2)(4n+3)} \left(\frac{r}{a}\right)^{4n+2} \sin\Bigl((4n+2)(\theta - \pi/4)\Bigr)\,. \end{aligned} \tag{43}$$

From this, a streamfunction can be constructed for the particle displacements inside the skull:

$$\begin{aligned} \psi \;=\; & \epsilon_0 a^2 \omega^2 \frac{8}{\pi} \cos\Bigl(\omega(t - t_0)\Bigr) \\ & \times \sum_{n=0}^{\infty} \frac{(-1)^n}{(4n+1)(4n+2)(4n+3)} \left(\frac{r}{a}\right)^{4n+2} \cos\Bigl((4n+2)(\theta - \pi/4)\Bigr) \end{aligned} \tag{44}$$

Instantaneous contours of p and ψ are plotted in figure 8.

The pressure scales as

$$\Delta p \sim \epsilon_0 \rho a^2 \omega^2 \sim \frac{\epsilon_0 K}{a^2}\,, \tag{45}$$

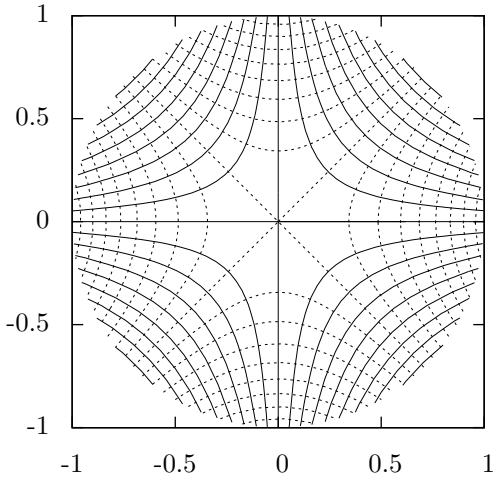

Figure 8: Instantaneous isobars (dashed lines) and particle pathlines (continuous lines) during oscillations using the simple skull model, plotted by taking contours of (43) and (44) respectively.

and has the largest amplitude adjacent to the hinges. An estimate for ϵ_0 is obtained by balancing the typical kinetic energy $\frac{1}{2}(\rho\pi a^2)V^2$ in a skull moving with uniform velocity V before a collision with the peak elastic energy $\frac{1}{2}4K(2\epsilon_0)^2$ in the hinges in the oscillatory mode afterwards. This yields

$$\epsilon_0 \sim \sqrt{\frac{\rho a^2 V^2}{K}}\,. \tag{46}$$

Using this estimate, we obtain

$$\Delta p \sim \frac{\sqrt{\rho K}V}{a} \tag{47}$$

consistent with (9) For a typical collision speed of 30 mph ($13\,\mathrm{ms}^{-1}$), the values in table 1 give an estimate of the pressure perturbations of the order of 10^5 Pa.

4 Pressure wave propagation and reflection in the ONSAS

Having considered how a deflection of the skull can lead to an increase in CSF pressure, we now consider a model for the flow of CSF along the ONSAS towards the eye. In particular, we consider an analytical model for the propagation of a CSF pressure pulse generated by a rapid skull motion (Sec. 4.1), demonstrating that this wave will steepen and form an elastic jump and examine its reflection at the ONSAS terminus (Sec. 4.2). Finally, we characterise the change in amplitude of this wave upon reflection using full numerical simulations (Sec. 4.3).

4.1 The model

We consider a 2D cross-section through the ONSAS oriented parallel to the optic nerve. We model the optic nerve and Pia mater as rigid, flat, impermeable surface forming one wall of the channel. We denote x and y as the directions along and normal to this surface oriented into the ONSAS as shown on Fig. 9(b).

We model the dura mater and arachnoid membrane as a single elastic sheet with a constitutive law linking CSF pressure and displacement derived in Sec. 2.4. Under healthy conditions we assume that this membrane is in some reference configuration $y = H(x)$, which correlates to a CSF pressure in the normal physiological range. In general we denote the position of the dura as $y = h(x, t)$. The setup of the model is shown in Fig. 9(b).

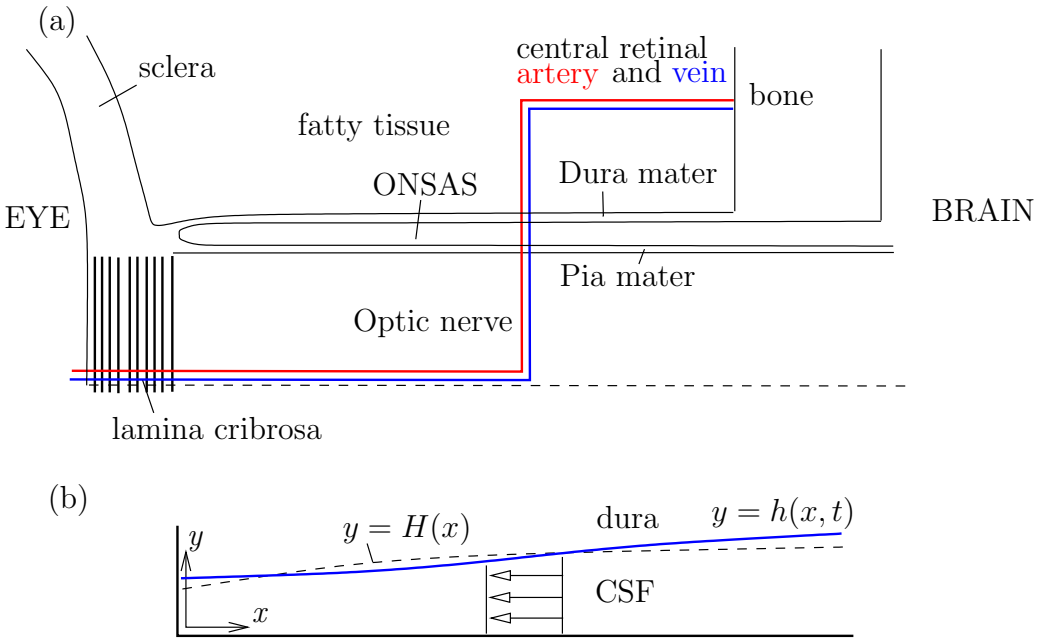

Figure 9: (a) Sketch of the geometry within the ONSAS (b) Setup of the mathematical model for the flow of CSF along the ONSAS

We assume the CSF can be modelled as ideal fluid with density ρ_c. Denoting the 2D fluid velocity field in the ONSAS as $\mathbf{u} = (u, v)$ and the CSF pressure as $p(x, t)$, the flow is governed by the incompressible Euler equations

$$\nabla \cdot \mathbf{u} = 0, \tag{48a}$$

$$\mathbf{u}_t + \mathbf{u} \cdot \nabla \mathbf{u} = -\frac{1}{\rho_c} \nabla p. \tag{48b}$$

The flow is subject to the no-penetration condition $v = 0$ on the interface $y = 0$, and kinematic and continuity of normal stress conditions on the dura

$$v = h_t + u h_x, \tag{49a}$$

$$p = \mathcal{P}(h), \tag{49b}$$

where $\mathcal{P}$ is the constitutive law fitted in (3) with $h = H + d$.

Assuming that the flow can be modelled as inviscid, the propagation of the elastic jump generated by the shock along the ONSAS can be approximated by the shallow-water equations and a tube law, which relates the cross-sectional width h to the local transmural pressure p [15], i.e.

$$h_t + (uh)_x = 0, \tag{50a}$$

$$u_t + u u_x = -\frac{1}{\rho_c} p_x, \tag{50b}$$

$$p = \mathcal{P}(h). \tag{50c}$$

Disturbances propagate at the dimensional wave-speed c satisfying

$$c^2 = \frac{h}{\rho_c} \frac{d\mathcal{P}}{dh}. \tag{50d}$$

The wavespeed in the ONS is estimated from $c^2 = (h/\rho_c)(\Delta p/\Delta h)$ to be $c \approx 2.5\,\mathrm{m/s}^2$.

4.2 Analytical solution for uniform width ONSAS

In this section, an analytical solution to the system (50) is sought. The ONSAS is modelled as an elastic-walled channel of uniform width $H = h_0$ at uniform pressure $p = p_0$ (figure 11a). The system of

(a) Initial (undisturbed) ONSAS

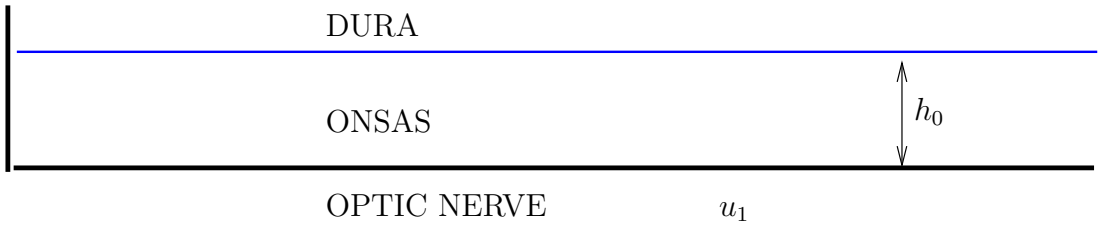

(b) elastic jump propagation along a uniform elastic-walled channel

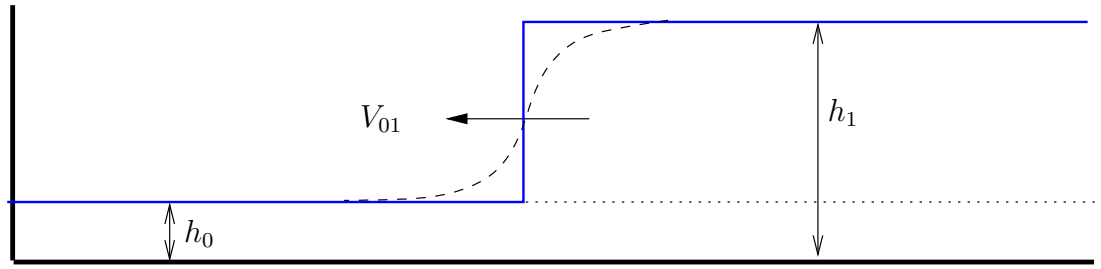

(c) reflection of an elastic jump at boundary

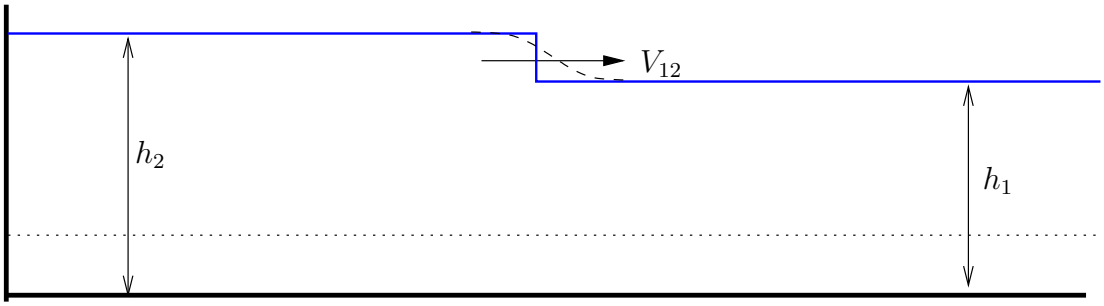

Figure 10: (a) Sketch of the geometry within the ONSAS (b) Setup of the mathematical model for the flow of CSF along the ONSAS

equations is solved using the methods of characteristics using the following Riemann invariants:

$$R_\pm = u \pm \int \frac{c}{h}\mathrm{d}h, \quad \frac{\mathrm{d}R_\pm}{\mathrm{d}t} = 0 \quad \text{on} \quad \frac{\mathrm{d}x}{\mathrm{d}t} = u \pm c. \tag{51}$$

4.2.1 Propagation of a pressure perturbation along ONSAS

We model a sudden rise in CSF pressure in the brain. This is communicated to the ONS via a short relatively rigid-walled channel where the ON passes through the skull. We neglect the pressure losses across this region and therefore prescribe p at the inlet of the ONS ($x = L$). The initial excitation caused by the shock is therefore modelled as a jump in pressure from $p = p_0$ to $p = p_1$, where p_1 and h_1 are linked by the tube law. The CSF is taken to be at rest initially with $u = 0, p = p_0$. The elastic jump advances at the speed V_{01}, as depicted in figure 11(b). The Rankine–Hugoniot conditions of conservation of mass and momentum across the elastic jump are applied, with $h = h_0$, $u = 0$, $p = p_0$ ahead of the shock, and $h = h_1$, $u = u_1$, $p = p_1$ behind the shock, i.e.

$$(u_1 - V_{01})h_1 = -V_{01}h_0 \tag{52a}$$

$$\tfrac{1}{2}\rho_c(u_1 - V_{01})^2 + p_1 = \tfrac{1}{2}\rho_c(-V_{01})^2 + p_0. \tag{52b}$$

The first equation yields:

$$u_1 = V_{01}\left(1 - \frac{h_0}{h_1}\right), \tag{53}$$

which leads to the expressions for u_1 and V_{01}:

$$V_{01}^2 = \frac{2\,(p_1 - p_0)}{\rho_c\left(1 - \frac{h_0^2}{h_1^2}\right)}, \qquad u_1^2 = \frac{2\,(p_1 - p_0)\left(1 - \frac{h_0}{h_1}\right)}{\rho_c\left(1 + \frac{h_0}{h_1}\right)}. \tag{54}$$

As a result, $u_1^2 < V_{01}^2$ for $h_0 < h_1$.

4.2.2 Reflection of a finite pressure perturbation along ONSAS

In order to take into account the temporality of the initial excitation and calculate the duration of the spike in pressure at the rigid wall and the length of the region affected by it, the excitation at the inlet is modelled as a constant pressure pulse of amplitude p_1 and duration Δt_0. As a result, the disturbance is a shock wave followed by a rarefaction wave. As described in the previous section, the reflection of the shock at the rigid wall at $t_1 = L/V_{01}$, where L is the length of the channel, creates a region of high pressure. As the wave changes its direction of propagation the reflected shock meets the rarefaction wave. The aim of the following analysis is to model the reflection of the pressure perturbation anteriorly and to calculate the length l_p of the region of high pressure and the duration t_p of the high pressure at the scleral cul-de-sac, which is here modelled as a rigid wall. The key quantities that determine the behaviour of the system are the speed of the back of the rarefaction wave c_0 given by the tube law; the speed of the front of the rarefaction wave $u_1 + c_1$, given respectively by equations (54) and the tube law; the speed of the initial shock V_{01}, given by equation (54); and the speed of the reflected shock V_{12}, which is calculated below.

After reflection, the elastic jump travels at the speed V_{12}, with $V_{12} < 0$ to account for the direction of the motion away from the boundary. Behind the shock, $h = h_2$, $p = p_2$ and $u = u_2 = 0$, and the shock advances into $h = h_1$, $u = u_1$, $p = p_1$. The Rankine–Hugoniot conditions become:

$$(u_1 - V_{12})h_1 = -V_{12}h_2 \tag{55}$$

$$\tfrac{1}{2}\rho(u_1 - V_{12})^2 + p_1 = \tfrac{1}{2}\rho(-V_{12})^2 + p_2, \tag{56}$$

which lead to

$$V_{12}^2 = \frac{2(p_2 - p_1)}{\rho(\frac{h_2^2}{h_1^2} - 1)}. \tag{57}$$

We are primarily interested in the amplification of pressure at the rigid boundary, i.e.

$$K = \frac{p_2}{p_1} = 1 + \frac{(h_1 - h_0)(h_2 + h_1)}{(h_1 + h_0)(h_2 - h_1)}. \tag{58}$$

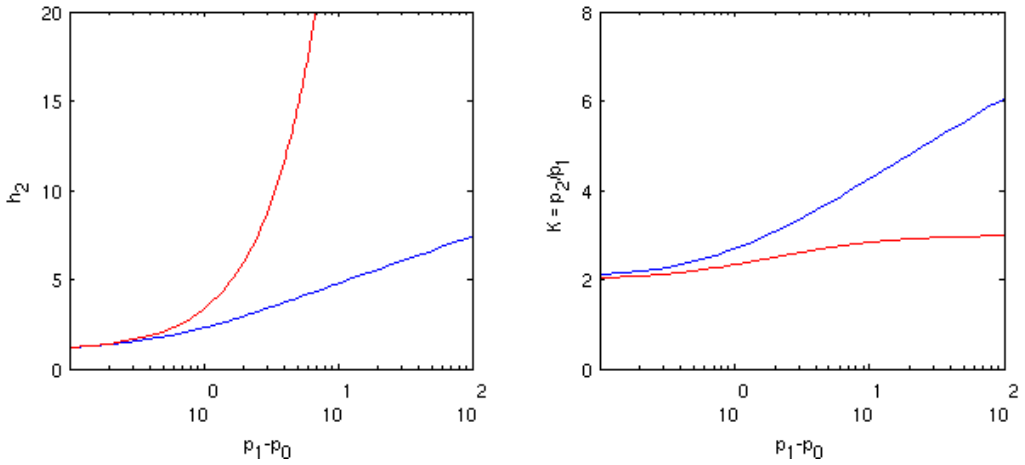

Figure 11: An elastic jump along a flexible-walled channel: the channel width and pressure amplification are plotted versus the input pressure difference. The red curve is computed for a linear tube law and the blue curve for a nonlinear tube law representing a tube that stiffens on inflation.

This relationship is illustrated in figure 11.

When the tube law is linear, with $p = k(h - h_0)$, the stiffness k cancels from the pressure ratio and h_2 satisfies:

$$h_2 = \frac{3h_1^2 - h_0 h_1}{h_0 + h_1}. \tag{59}$$

In order to calculate l_p and t_p, the length of the channel L and the duration of the pulse Δt_0 need to be specified. The reflected shock wave meets the rarefaction wave at the time t_2, and at the distance l_2 from the wall. The behaviour of the finite pressure perturbation can be illustrated by a simple characteristic diagram, shown in figure 12. Recalling that $t_1 = L/V_{01}$,

$$t_2 = \frac{L + (u_1 + c_1)\Delta t_0 - t_1 V_{12}}{-V_{12} + u_1 + c_1} \tag{60}$$

$$l_2 = (u_1 + c_1)(t_2 - \Delta t_0). \tag{61}$$

Assuming that its speed is not affected by meeting the reflected shock, the rarefaction wave meets the wall at t_3, so that $t_p = t_3 - t_1$ can be calculated to be

$$t_p = \frac{L - l_2}{u_1 + c_1} + t_2 - t_1. \tag{62}$$

The length l_p satisfies $l_p = L - l_2$ so that

$$l_p = L - (u_1 + c_1)(t_2 - \Delta t_0). \tag{63}$$

For a linear tube law, assuming that the CSF pressure at rest is $p_0 = 11$mmHg$= 1.5$kPa, that the pressure excitation is $p_1 = 5$kPa and that the optic nerve is about 20mm long, physically meaningful values for l_p and t_p are only obtained for an initial excitation $\Delta t_0 \geq 3.46$ms, which correspond to frequencies of approximately $\omega \leq 290 s^{-1}$. For $\omega \leq 43 s^{-1}$, $l_p > L$, and therefore non-physical values are obtained. This suggests that given the modelling assumptions proposed here and the set of data used, the resonance frequency of the baby head following a shock at $13 ms^{-1}$ ($\omega = 30 s^{-1}$) leads to non-physical results. If the pressure rise p_1 is smaller than 200Pa, the resonance frequency does give physical values of $0 \leq l_p \leq 12 mm$, however the pressure surge measured during a simple sneeze suggests that p_1 needs to be larger than 200Pa.

Within the range of physically significant results, l_p and t_p vary quasi-linearly with Δt_0. For $p_1 =$ 10kPa and $\Delta t_0 = 0.0025 s$:

$$l_p = 0.3\text{mm} \tag{64}$$

$$t_p = 0.6\text{ms}, \tag{65}$$

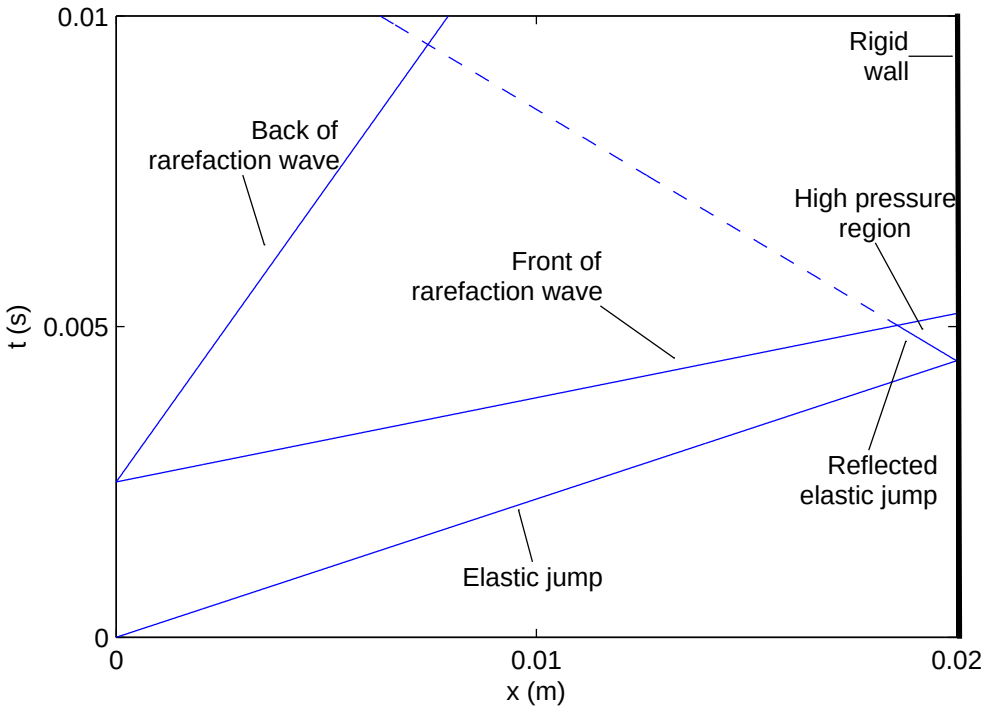

Figure 12: A simple characteristic diagram showing the behaviour of the finite pressure perturbation as it interacts with a rigid wall. The elastic jump reflects off the wall and meets the incoming rarefaction wave. The dashed line indicates the path the reflected jump would take if it did not meet the rarefaction wave. The tube law is taken to be linear, $p = k\,(h - h_0)$, with $k = 2.2\text{x}10^6$Pa/m and $h_0 = 5$mm, so that $h_1 \approx 5$mm and $h_2 = 13.2$mm. The density is taken to be $\rho = 1000\text{kg/m}^3$. The length of the channel is taken to be $L = 20$mm and the pressure perturbation is taken to last $t_0 = 0.0025$s. Indicated in the diagram is the high pressure region, where $p = p_2$; here we take $p_0 = 1463$Pa, which is equivalent to $p_0 = 11$mmHg; the initial pressure perturbation is taken to be $p_1 = 10^4$Pa, so that $p_2 = 2.82\text{x}10^4$Pa.

which is physically plausible but difficult to test given the limited amount of quantitative data available from histologic studies.

4.3 Numerical simulations

The shallow water model admits discontinuties in the width of the ONSAS (an elastic jump), which is difficult to capture numerically without a specially adapted scheme [3]. Instead we modify the model in two ways to make solving (50) more numerically tractable. Firstly, we modify the elastic wall model to also include an elastic pre-stress (or tension T_d), so that the normal stress balance across the membrane (49b) becomes

$$p = p_e(x) + \mathcal{P}(h) - T_d h_{xx}. \tag{66}$$

This normal stress balance also incorporates an external pressure gradient $p_e(x)$ in the medium surrounding the dura. Secondly, we assume that the CSF has Newtonian rheology with a small viscosity, μ.

For simulations we set the baseline thickness of the CSF space to be uniform $H(x) = h_0 = 0.7$mm and the length of the CSF space in the region of interest as $L = 27$mm. We further define the aspect ratio of the channel as $\epsilon = h_0/L$. Further parameter values are listed in Table 1.

We derive a typical velocity of the CSF pulse along the ONSAS assuming a balance between the driving pressure and the fluid inertia, so that $U_0 = (\Delta p/\rho)^{1/2}$. For example, based on the pressure perturbation predicted by Sec. 3, $\Delta P = 10^5$Pa, and assuming $\rho_c = 1000\text{kg/m}^3$ (water), we obtain an estimate of the flow speed of $U_0 = 10$m/s.

We define dimensionless variables by scaling the coordinate system $(x, y) = (L\tilde{x}, h_0\tilde{y})$, velocities on $(u, v) = (U_0\tilde{u}, \epsilon U_0\tilde{v})$, time on L/U_0 and pressures according to

$$p = p_0 + \Delta p\tilde{p} \tag{67a}$$

$$\mathcal{P} = p_0 + \Delta p\tilde{\mathcal{P}}. \tag{67b}$$

This rescaling results in three dimensionless parameters

$$\tilde{K} = \epsilon^2 \frac{K}{\rho U_0^2}, \qquad \tilde{T} = \epsilon^2 \frac{T_d}{\rho U_0^2 h_0}, \qquad \tilde{R} = \epsilon \frac{\rho U_0 H}{\mu} \tag{68}$$

To leading order in ϵ, the Navier–Stokes equations reduce to modified shallow-water equations involving a coupled system of two PDEs for the dimensionless channel thickness $\tilde{h}(\tilde{x}, \tilde{t})$ and the channel flow rate $\tilde{q}(\tilde{x}, \tilde{t})$. However, this system is not closed and so to overcome we assume the flow velocity profile takes the form of a von-Karman Pohlhausen approximation, being everywhere parabolic of the form

$$\tilde{u} = \frac{6\tilde{q}\tilde{y}(\tilde{h} - \tilde{y})}{\tilde{h}^3}, \qquad \text{where} \qquad \tilde{q} = \int_0^{\tilde{h}} \tilde{u}\, \mathrm{d}\tilde{y}. \tag{69}$$

We assume the external pressure gradient takes the dimensionless form

$$\tilde{p}_e = -\frac{12}{\tilde{R}}\tilde{x}. \tag{70}$$

The resulting system was previously presented by [18] in the form

$$\tilde{h}_{\tilde{t}} + \tilde{q}_{\tilde{x}} = 0, \tag{71a}$$

$$\tilde{q}_{\tilde{t}} + \frac{6}{5}\left(\frac{\tilde{q}^2}{\tilde{h}}\right)_{\tilde{x}} = -\tilde{h}\tilde{\mathcal{P}}_{\tilde{x}} + \frac{12}{\tilde{R}}\left(\tilde{h} - \frac{\tilde{q}}{\tilde{h}^2}\right), \tag{71b}$$

$$\tilde{p} = \tilde{\mathcal{P}} - \tilde{T}\tilde{h}_{\tilde{x}\tilde{x}}. \tag{71c}$$

where $\tilde{\mathcal{P}}$ is defined by (66). These equations hold on the domain $0 < \tilde{x} < 1$, where $\tilde{x} = 1$ represents the edge of the orbit and $\tilde{x} = 0$ represents the rigid terminus in the ONSAS (see figure 9a). To mimic a traumatic event we apply a large pressure perturbation at $\tilde{x} = 1$, discussed in more detail below. We also apply zero slope conditions at the lamina cribrosa ($\tilde{x} = 0$) and fixed membrane height at the ONSAS inlet ($\tilde{x} = 1$). To close the system we enforce no flow of CSF through the lamina cribrosa/sclera $\tilde{q}(0, \tilde{t}) = 0$.

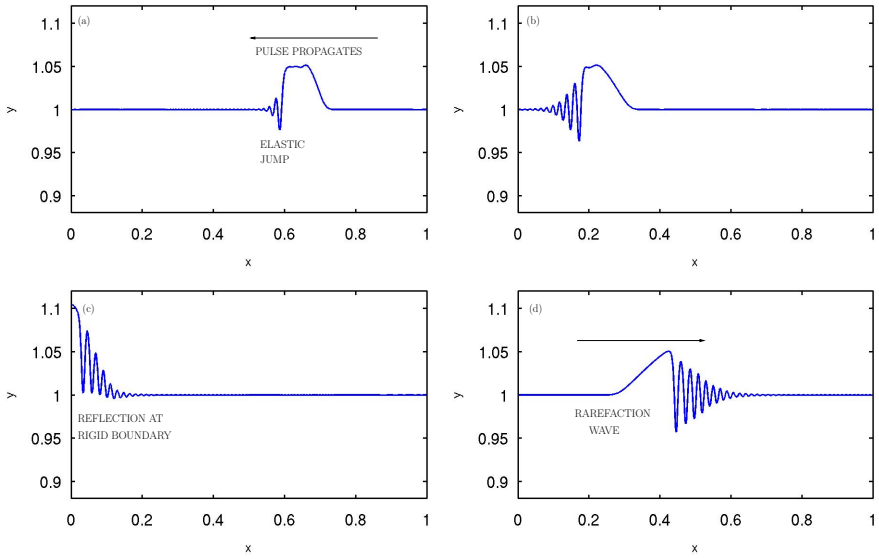

Figure 13: Reflection of an elastic jump at a rigid terminus of the ONSAS using Linear constitutive law (73) with $\tilde{K}_l = 100$: (a,b) propagation of the CSF pulse towards the eye; (c) reflection of the pulse at the lamina cribrosa; (d) propagation of reflected wave towards the brain.

In the simulations presented below we hold $\tilde{T} = 10^{-4}$ and $\tilde{R} = 500$.

We apply a pressure perturbation at the upstream end of the channel over a (dimensionless) period τ in the form

$$\tilde{p}_u = \sin^2(\Omega\tilde{t}) \qquad 0 < \tilde{t} \leq \tfrac{1}{4}\tau, \tag{72a}$$

$$\tilde{p}_u = 1 \qquad \tfrac{1}{4}\tau < \tilde{t} \leq \tfrac{3}{4}\tau, \tag{72b}$$

$$\tilde{p}_u = \sin^2(\Omega(\tilde{t} + \tfrac{1}{2}\tau)) \qquad \tfrac{3}{4}\tau < \tilde{t} \leq \tau, \tag{72c}$$

$$\tilde{p}_u = 0, \qquad \tilde{t} > \tau. \tag{72d}$$

where $\Omega = 2\pi/\tau$. In simulations below we set $\Omega = 200$.

For convenience we simplify the constitutive law for the dura mater, assuming

$$\tilde{\mathcal{P}}(\tilde{h}) = \tilde{K}_l(\tilde{h} - 1). \tag{73}$$

The upstream pressure perturbation generates a pressure pulse which propagates along the ONSAS towards the eye. Four snapshots from a typical example are shown in Fig. 13(a-d) for $\tilde{K}_l = 100$. As this pulse encounters the rigid end of the ONSAS it is reflected back toward the brain; since the constitutive law is linear (73) we find that the pressure is amplified by a constant factor of 2. However, this constitutive law is a poor reflection of the clinical data (see figure 3), so we aim to analyse wave reflections using the nonlinear constitutive law (3) in future work.

5 Discussion

We have presented here a set of related models seeking to understand the generation and evolution of a rapid rise in CSF pressure arising from a traumatic injury to an infant skull.

The model for the skull as a hinged circular shell is based on a physical balance between the stiffness of the sutures between the skull plates and the inertia of the tissue within it. The model exploits an idealised geometry and is restricted to small amplitudes. However it demonstrates the factors determining the likely timescale over which a spike in CSF arises and estimates its magnitude. Future studies should address more realistic geometries and account for nonlinear deformations; finite element simulations in the literature may be relevant [17, 11, 12].

In the model of the ONSAS we exploited its slender geometry to descibe the internal flow using a spatially one-dimensional representation of mass and momentum conservation that resembles the shallow

water equations, coupled to a tube law that relates the CSF pressure to local deformations of the dura. Measurements indicate that the tube law is strongly nonlinear (figure 3). The governing equations are sufficiently simple for the disturbance to be described semi-analytically in terms of characteristics. This makes it possible to estimate the magnitude and duration of the zone of elevated pressure at the closed end of the ONSAS (figures 11 and 12). In our time-dependent simulations, however, we restricted attention to a linear tube law. The dynamics of the process was captured using simulations in which the tube law was extended to account for axial tension, which induces a train of dispersive waves (figure 13) but which nevertheless illustrates the localised elevated pressure at the peripheral end of the ONSAS.

5.1 Relation of results to healthcare technologies

The eye provides a window to the brain and it may be imaged through a variety of modalities. Haemorrhage is a potential indicator to healthcare professionals of trauma to infants. Improved understanding of the mechanisms leading to bleeding in and around the eye is therefore valuable for child safeguarding, family protection and criminal justice. The present study focuses on a particular form of bleeding that is reported in instances of non-accidental head injury. It is our intention to refine the model and publish the findings in the ophthalmology literature to make the findings available to healthcare professionals.

5.2 Relation of results to 3Rs

Large animal models have been shown to offer advantages over rodent models in replicating specific mechanisms, morphology and maturational stages relevant to age-dependent brain injury responses [6]. For example, piglets have been used to mimic human brain injury due to (i) impact and (ii) rotational mechanical trauma via (i) direct impact upon the cortex of the brain causing brain indentation [7] or (ii) via sudden rapid head rotation [16, 9], and indeed sudden very rapid head rotations in neonatal piglets have been shown to lead to retinal haemorrhage [4]. The use of over 200 piglets has been reported in literature from the last 5 years, and these experiments involve severe injury and trauma to the animals. Furthermore, despite the advantages of large animal models, practicalities and size mean that a large number of rodents are also used to model brain injury. For example, neonatal rat pups have been exposed to hypoxia in an atmosphere of 5% oxygen in order to determine whether hypoxia leads to retinal damage [10]. Nevertheless, better proxies for human developmental anatomy and pathophysiology are desperately needed because of the biologically unique characteristics of the developing human infant and young child. Mathematical and computational models complement such approaches by investigating different mechanisms of injury *in silico*. Our results suggest that there is potential for mathematical and computational models to reduce the need for animal experimentation, while providing improved guidance for clinical diagnosis, with implications for legal assessments in cases of potential child abuse.

Acknowledgements

We are grateful to the sponsors and participants of the 2014 NC3Rs/POEMS Network Maths Study Group held at the University of Cambridge for supporting this study and contributing to discussions. We particularly thank Drs Bindi Brook, Alex Foss, John McCarthy and Jennifer Siggers for their input.

References

[1] Agrawal S & Brierley J, Optic nerve sheath measurement and raised intracranial pressure in paediatric traumatic brain injury. Eur. J. Trauma Emerg. Surg. 38:75–77 (2012)

[2] Berkouk K, Carpenter, PW & Lucey AD, Pressure wave propagation in fluid-filled co-axial elastic tubes part 1: basic theory. J. Biomech. Eng. 125:852–856 (2003)

[3] Brook BS, Falle SAEG & Pedley TJ, Numerical solutions for unsteady gravity-driven flows in collapsible tubes: evolution and roll-wave instability of a steady state. J. Fluid Mech. 396:223–256 (1999)

[4] Coats B, Binenbaum C, Peiffer RL, Forbes BJ & Margulies SS, Ocular hemorrhages in neonatal porcine eyes from single, rapid rotational events. Invest. Ophthalmol. Vis. Sci. 51:4792–4797 (2010)

[5] Coats B & Margulies SS, Material properties of human infant skull and suture at high rates. J. Neurotrauma. 23:1222–1232 (2006)

[6] Duhaime AC, Large animal models of traumatic injury to the immature brain. Dev. Neurosci. 28:380–387 (2006)

[7] Duhaime AC, Margulies SS, Durham SR, O'Rourke MM, Golden JA, Marwaha S & Raghupathi R, Maturation-dependent response of the piglet brain to scaled cortical impact. J. Neurosurg. 93:455–462 (2000)

[8] Emerson MV, Jakobs E & Green WR, Ocular autopsy and histopathologic features of child abuse. Ophthalmology 114:1384–1394 (2007)

[9] Ibrahim NG, Ralston J, Smith C & Margulies SS, Physiological and pathological responses to head rotations in toddler piglets. J. Neurotrauma 27:1021–1035 (2010)

[10] Kaur C, Sivakumar V, Foulds WS, Luu CD & Ling, EA, Cellular and vascular changes in the retina of neonatal rats after an acute exposure to hypoxia. Invest. Ophthalmol. Vis. Sci. 50:5364-5374 (2009)

[11] Li Z, Hu J, Reed MP, Rupp JD, Hoff CN, Zhang J & Cheng B, Development, validation and application of a parametric pediatric head finite element model for impact simulations. Ann. Biomed. Eng. 39:2984–2997 (2011)

[12] Li Z, Luo X & Zhang J, Development/global validation of a 6-month-old pediatric head finite element model and application in investigation of drop-induced infant head injury. Comp. Meth. Prog. Biomed. 112:309–319 (2013)

[13] Mena OJ, Paul I & Reichard RR, Ocular findings in raised intracranial pressure: a case of Terson syndrome in a 7-month-old infant. Am. J. Forensic Med. Path. 32:55–57 (2011).

[14] Muller PJ & Deck JHN, Intraocular and optic nerve sheath hemorrhage in cases of sudden intracranial hypertension. J. Neurosurg 41:160–166 (1974)

[15] Pedley TJ, The fluid mechanics of large blood vessels, Cambridge University Press (1980).

[16] Raghupathi R, Mehr M, Helfaer MA, Margulies SS, Traumatic axonal injury is exacerbated following repetitive closed head injury in the neonatal pig. J. Neurotrauma 21:307–316 (2004)

[17] Roth S, Vappou J, Raul J-S & Willinger R, Child head injury criteria investigation through numerical simulation of real world trauma. Comp. Meth. Prog. Biomed. 93:32–45 (2009)

[18] Stewart PS, Waters SL & Jensen OE, Local and global instabilities of flow in a flexible-walled channel. Eur. J. Mech. B 28:541–557 (2009)

[19] Walsh FB & Hedges TR, Optic nerve sheath hemorrhage. Am. J. Ophthalmol. 34:509–527 (1951)

[20] Wirtschafter J, Weissgold DJ, Budenz DL, Hood I & Rorke LB, Ruptured vascular malformation masquerading as battered/shaken baby syndrome: a nearly tragic mistake. Surv. Ophth., 39:509–512 (1995).

[21] Xie, X, Zhang X, Fu J, Wang H, Jonas JB, Peng, X, Tian G et al., Noninvasive intracranial pressure estimation by orbital subarachnoid space measurement: the Beijing Intracranial and Intraocular Pressure (iCOP) study. Crit. Care 17:R162 (2013)